Full Length Article

Silicon @ nitrogen-doped porous carbon fiber composite anodes synthesized by an in-situ reaction collection strategy for high-performance lithium-ion batteries

Yue Ouyang[a,1], Xiaobo Zhu[a,1], Fei Li[a], Feili Lai[a], Yue Wu[b], Yue-E Miao[a,*], Tianxi Liu[a]

[a] State Key Laboratory for Modification of Chemical Fibers and Polymer Materials, College of Materials Science and Engineering, Innovation Center for Textile Science and Technology, Donghua University, 2999 North Renmin Road, Shanghai 201620, PR China
[b] Research Center for Analysis and Measurement, Donghua University, Shanghai 201620, PR China

A B S T R A C T

Silicon (Si)/carbon nanocomposites have attracted extensive interests as emerging electrode materials in lithium-ion batteries (LIBs) due to their numerous premium features of high capacity, good conductivity, excellent ductility and long cycle life. Herein, we introduce a novel nitrogen-doped porous carbon fiber framework entrapped with Si nanoparticles (Si@NPCNF) by an improved electrospinning strategy with an in-situ reaction bath of pyrrole as the special collector. It is interesting that the in-situ collected polypyrrole (PPy) coated Si/PMMA precursor fibers show uniform diameter around 1.2–1.5 μm with three-dimensional (3D) interconnected porous structures. After heat treatment at 850 °C, the resulted Si@NPCNF nanocomposite with high porosity and large surface area, can effectively relieve the severe volume expansion of silicon to reduce the pulverization of Si anode during the discharge/charge processes. Furthermore, the thin N-doped carbon layer derived from PPy can largely improve the conductivity of Si anode and shorten the Li$^+$ diffusion distance. Meanwhile, the 3D porous structure can efficiently prevent Si from directly contacting with electrolyte to improve the cycling stability of LIBs. Therefore, the Si@NPCNF nanocomposite exhibits outstanding electrochemical performance which delivers a high initial capacity of 1521 mA h g^{-1} at 0.1 A g^{-1}, a good rate capability of 648 mA h g^{-1} at 2 A g^{-1} and excellent cycle stability of 515.5 mA h g^{-1} after 200 cycles at 1 A g^{-1}, being promising as a high-performance anode material for lithium-ion batteries.

1. Introduction

Nowadays, lithium-ion batteries (LIBs) have been considered as one kind of the most promising energy storage devices due to their excellent environmental compatibility, long cycle life, low self-discharge and high energy density [1–3]. As a result, they have become common power sources in all aspects of life, such as mobile electronic equipment, electric vehicles, and large-scale stationary energy storage systems [4,5]. Traditionally, graphite is the commercialized anode material for LIBs, which is however limited to its low theoretical capacity of 372 mA h g^{-1} [6–8]. Thus, researchers have been actively worked on finding new electrode materials with even higher specific capacity, energy density and cyclability, along with lower cost and security risks to meet the rapid development of modern technology [9,10].

Among various emerging anode materials, silicon (Si) is considered as one of the most promising materials to replace graphite. With

environmental friendliness and abundant reserves in nature, Si exhibits an extremely high theoretical capacity of 4200 mA h g^{-1} and a relatively low working potential of 0.2 V (vs Li/Li$^+$) [11–15]. Nevertheless, Si electrodes cannot be used on large scales in commercial applications, owing to their poor electrical conductivity (*i.e.*, 10^{-5}–10^{-3} S cm^{-1} under 25 °C) and large volume changes of 300–400% upon cycling [16]. These defects lead to the fact that the electrode materials are easily pulverized with serious capacity fading during alloying/dealloying processes. Furthermore, the unstable solid electrolyte interphase (SEI) film in turn accelerates the electrode destruction. Scientists have demonstrated that the large volume variations of the negative Si electrode would largely reduce the electrical contacts between the current collectors and active electrode materials, which further accelerates the irreversible side reactions with organic electrolyte [17]. Eventually after long-term cycling, the repeated volume changes may gradually crash the Si matrix, thereby leading to low cycling efficiency,

---

* Corresponding author.
  E-mail address: yuee_miao@dhu.edu.cn (Y.-E. Miao).
  [1] These authors contributed equally.

permanent capacity loss or even failure of the battery.

To eliminate the negative effects of its volume change, numerous efforts have been devoted in the development of Si-based composite electrodes with particular structures [15,16,18–22], such as porous Si nanoparticles, Si alloys, Si/carbon composites, Si/graphene composites, Si nanowires, and Si thin films. Although significant breakthroughs have been achieved in the improvement of the cycle life and rate capabilities of Si, many hindrances still exist to be overcome, especially the huge volume expansion upon alloying/dealloying of Si anodes [11,13,15,23,24]. The electrochemically inactive silicides in Si alloy anodes are reported to effectively reduce the volume changes and inhibit the pulverization of Si. However, the problems of mechanical fracture and growing side reactions of Si alloys, as well as the high cost of metals, have hindered their large-scale applications [25]. In comparison, porous carbon in Si/C composites can not only improve the electrical conductivity of Si anodes, but also act as the buffering substrates for Si expansion [26–30]. Nevertheless, the problems of the reformed SEI film and exhausted electrolyte due to the repeated cycling of the Si anode still exist. In order to make full use of the silicon anode with high theoretical capacity and further improve the cycling stability of LIBs, it is highly desirable to develop Si/C composites with unique porous structures, which can provide adequate void spaces for Si expansion as well as prevent Si from directly contacting and consuming the electrolyte to form stable SEI films.

In addition to the effective containment of the volume expansion by constructing porous carbonaceous materials [31], the heteroatom doping has been also found to effectively modify the functional groups on the surface of the carbon layer [32–35]. As a result, the electrical conductivity and storage capacity of carbonaceous materials will be significantly improved. Herein, one-dimensional (1D) Si-encapsulated polyvinyl pyrrolidone/polymethyl methacrylate (Si/PVP/PMMA) composite fibers have been directly electrospun into an in-situ reaction collection bath of pyrrole. Thus, the facile dissolution of PVP and in-situ polymerization of pyrrole on the surface of Si/PMMA fibers have been simultaneously realized to obtain polypyrrole (PPy) coated Si/PMMA (Si/PMMA@PPy) composite fibers with unique porous structures as illustrated in Fig. 1. Subsequently, the thermal treatment of Si/PMMA@ PPy was carried out to prepare the PPy-derived nitrogen-doped porous carbon fiber framework entrapped with Si nanoparticles, which is denoted as Si@NPCNF. It is interesting that the three-dimensional (3D) interconnected porous structure has been totally duplicated by the PPy-derived NPCNF framework, which is expected to behave as both the conductive and buffering template providing favorable conductive pathway for Li$^+$ diffusion and abundant voids to accommodate the huge volume change of Si nanoparticles. Benefiting from the advantageous features of high porosity and good conductivity within the 3D porous substrate, the Si@NPCNF composite exhibits excellent electrochemical performances as the anode material for LIBs, such as high initial capacity, long-term cycle stability, and excellent rate capability.
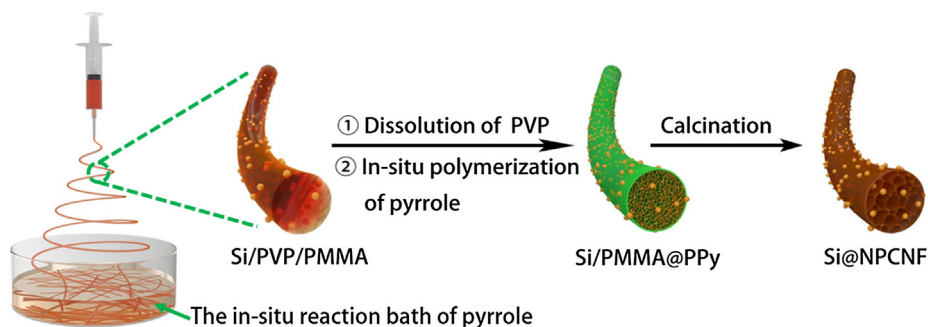
2. Experimental section

2.1. Materials

PVP (M$_w$ ≈ 1,300,000), PMMA (M$_w$ ≈ 350,000) and pyrrole were purchased from Sigma-Aldrich. Si nanoparticles were obtained from Shanghai St-Nano Science and Technology Co., Ltd. FeCl$_3$ and *N,N*-Dimethylformamide (DMF) were supplied by Sinopharm Chemical Reagent Co., Ltd. All the chemicals were of analytical grade and used without further purification.

2.2. Preparation of Si@NPCNF nanocomposites

First, Si nanoparticles, PVP, PMMA and DMF were mixed in glass bottles at different mass ratios of 1:4:16:180, 3:4:16:180 and 5:4:16:180, respectively, and stirred at room temperature for 12 h to obtain the precursor solutions with uniform dispersion of Si nanoparticles. After that, the precursor solution was loaded into a syringe equipped with a 0.5 mm needle and directly electrospun into the deionized water bath collector to prepare hydrophilic Si/PMMA fibers. During the electrospinning process, a voltage of 15 kV and a feeding rate of 0.8 mm min^{-1} were applied to the spinneret.

As PPy is one of the most commonly used N-rich conducting polymers, the as-spun Si/PMMA fibers were also directly collected in an aqueous acidic solution of pyrrole (0.7 mg mL^{-1} in 1 M hydrochloric acid) first. Then, 15 mM FeCl$_3$ was slowly added to the above solution to initiate the in-situ polymerization of pyrrole. The reaction was allowed to further proceed for 12 h at 2 ± 1 °C, thus resulting in the final product of Si/PMMA@PPy, in which PVP was already dissolved and removed by water. Subsequently, the products were calcinated under Ar atmosphere at 850 °C for 2 h to make PMMA completely decomposed and PPy converted into N-doped carbon fiber framework. As a result, the Si@NPCNF nanocomposites containing different loading amounts of Si nanoparticles are obtained, which are signed as Si-1@NPCNF, Si-2@NPCNF, Si-3@NPCNF, respectively. The NPCNF composite without Si nanoparticles was also prepared by the same method as illustrated in Fig. 1.

2.3. Characterizations

Morphology of the samples was observed with field-emission scanning electron microscope (FESEM, Ultra 55) and transmission electron microscope (TEM, Tecnai G2 20 TWIN). X-ray diffraction (XRD) patterns were obtained using an X'Pert PRO X-ray diffractometer at a current of 40 mA and voltage of 40 kV with Cu K$_\alpha$ radiation. X-ray photoelectron spectroscopy (XPS) was measured by Thermo Scientific ESCALAB 250Xi equipped with Al K$_\alpha$ X-ray source at an energy of 1486.6 eV. Brunauer-Emmett-Teller (BET) nitrogen adsorption/desorption isotherms were tested by using a Quantachrome Autosorb-iQ/MP®XR system. Thermogravimetric analysis (TGA) was performed on a TG 209 F1 Libra (Netzsch) under air atmosphere.
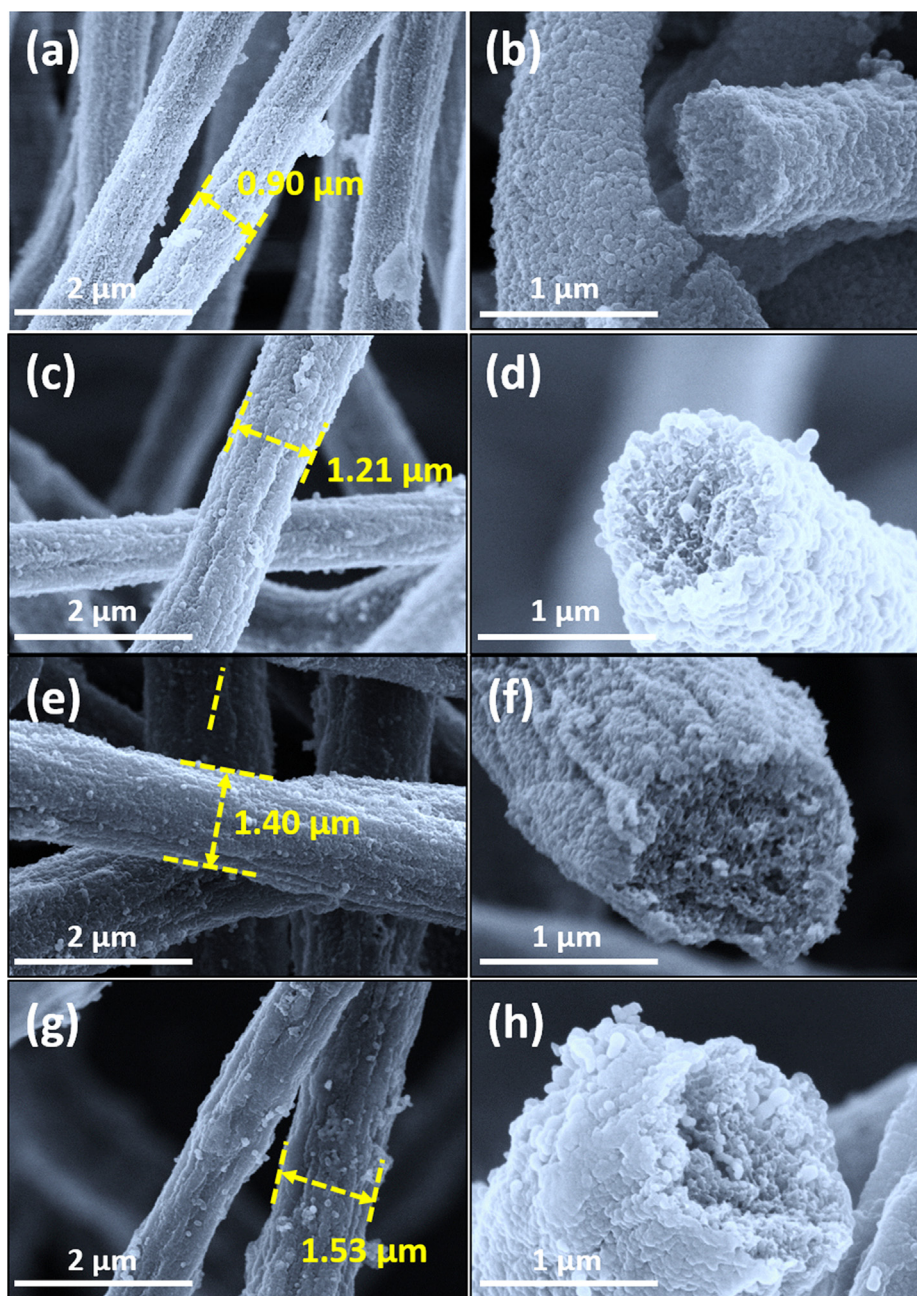

Fig. 1. Schematic showing the preparation of Si@NPCNF composites through an in-situ reaction collection bath.

Fig. 2. SEM images of (a,b) PMMA@PPy, (c,d) Si/PMMA-1@PPy, (e,f) Si/PMMA-2@PPy, (g,h) Si/ PMMA-3@PPy.

2.4. Electrochemical measurements

Primarily, the Si@NPCNF electrodes were prepared by casting the homogeneous slurry including 80 wt% Si@NPCNF, 10 wt% acetylene carbon black, and 10 wt% polyvinylidene fluoride (PVDF) binder on a copper foil. After drying in a vacuum oven at 80 °C for 12 h, the electrodes were punched into round films with 12 mm in diameter. The coin cells were assembled in an argon filled glove-box by using Celgard 2300 as the separator and lithium foil as the counter electrode. Cyclic voltammetry (CV) curves were carried out on an ARBIN BT2000 system in the voltage range of 0.01–1.5 V at a sweep rate of 0.1 mV s^{-1}. The galvanostatic discharge/charge tests of the cells were carried out between 0.01 and 1.5 V (vs. Li/Li^{+}) by the LAND 2001A battery testing system. Electrochemical impedance spectra (EIS) measurements were performed by an electrochemical workstation in the frequency range from 10^5 Hz to 0.01 Hz under the automatic sweep mode.

3. Results and discussion

As depicted in Fig. 1, Si/PMMA@PPy fibers are prepared through the direct collection of the intermediate Si/PVP/PMMA fibers in the reaction solution bath of pyrrole. Thus, the hydrophilic component of PVP can be efficiently removed to form porous Si/PMMA fibers while in-situ growth of PPy happens on the surface of the Si/PMMA fibers at the same time. As shown in Fig. S1, the mean diameter of the as-collected Si/PMMA fibers increases from 600 nm to 820 nm combining with increasing content of Si nanoparticles. Meanwhile, no obvious aggregates of Si nanoparticles are observed on the surface of the composite fibers under the low loading amounts of Si (Si/PMMA-1 and Si/PMMA-2, Fig. S1d and S1f) while large agglomerations of Si nanoparticles start to appear on the surface of Si/PMMA-3 (Fig. S1h), indicating that too large loading content of Si makes its dispersion very difficult. After the deposition of PPy by in-situ polymerization, the
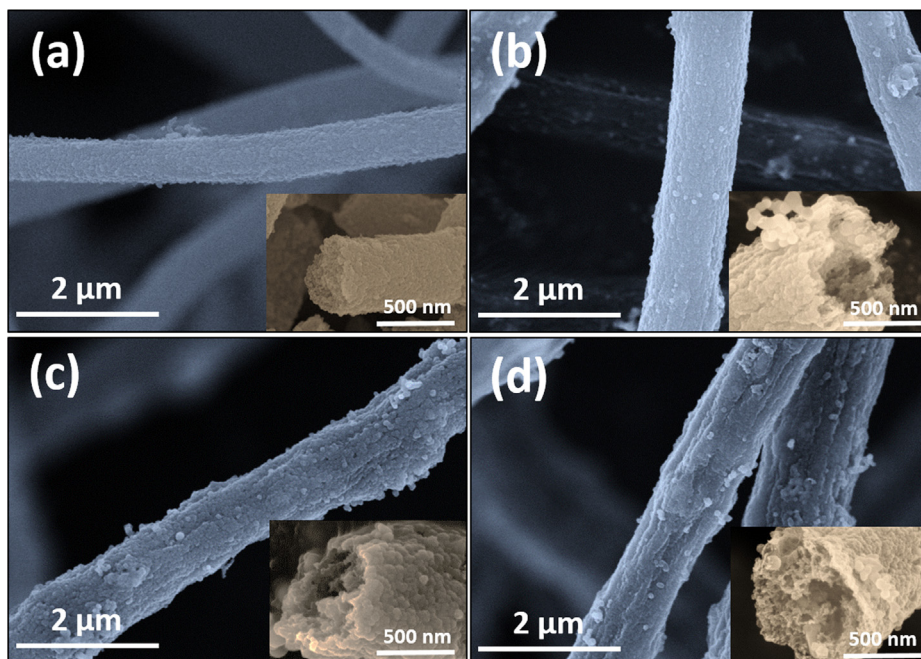
Fig. 3. SEM images of (a) NPCNF, (b) Si-1@NPCNF, (c) Si-2@NPCNF, and (d) Si-3@NPCNF.
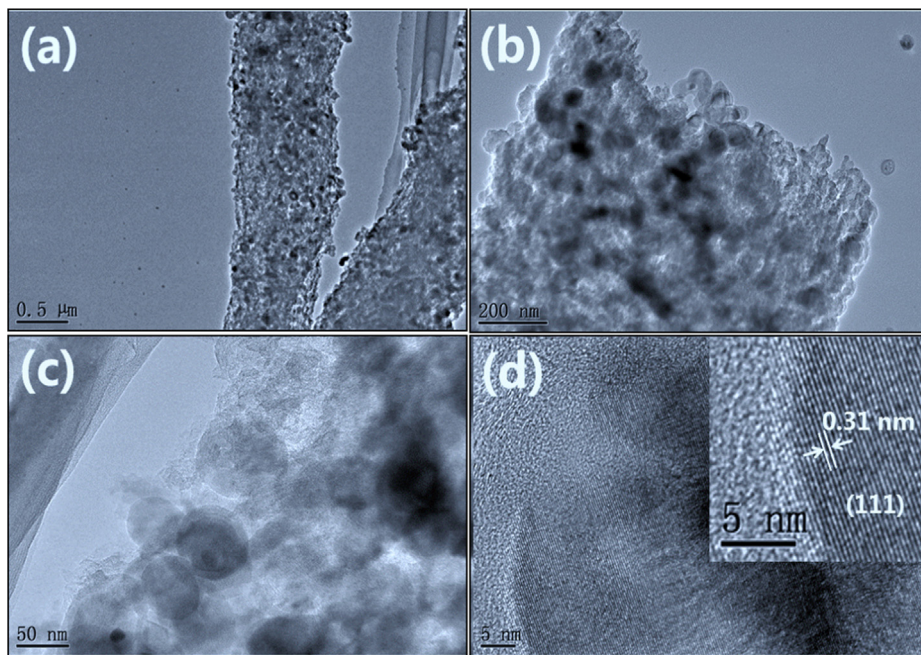

Fig. 4. (a) The typical TEM image of Si-2@NPCNF, (b-d) high magnification TEM images of Si-2@NPCNF. The inset of (d) shows the interplanar spacing of Si nanoparticles.

surfaces of Si/PMMA@PPy fibers become much rougher than those of Si/PMMA fibers due to the random nucleation and granular growth of the PPy coating as displayed in Fig. 2. The diameters of Si/PMMA-1@ PPy, Si/PMMA-2@PPy and Si/PMMA-3@PPy fibers are estimated to be 1.21, 1.40, and 1.53 μm, respectively. It is evident that the thickness of PPy coating is all over 300 nm while the porous structure inside the composite fibers are completely maintained, which guarantees the subsequent acquisition of the Si-based composite electrode with rich porous structures. Being a useful conducting carbon source, the PPy coatings are successfully turned into nitrogen-doped porous carbon nanofibers while the PMMA template is totally decomposed under the high-temperature treatment as shown in Fig. 3. It can be also clearly

observed that Si nanoparticles are evenly distributed on the surface and inside of the NPCNF frameworks, which are beneficial for the rapid transport of electrons/electrolytes and accommodation of the severe volume expansions of Si nanoparticles during the later discharge/ charge processes.

TEM images of Si@NPCNF are further obtained to get inside the pore structures and distribution of Si nanoparticles along the NPCNF fibers. As expected, Fig. 4a and 4b prove a uniform diameter around 500 nm for the Si@NPCNF composite fibers. Especially, the dark-colored Si nanoparticles are observed with very uniform distribution within the NPCNF fibers while the almost transparent areas are the cavities mainly formed by the removal of PVP in the reaction solution
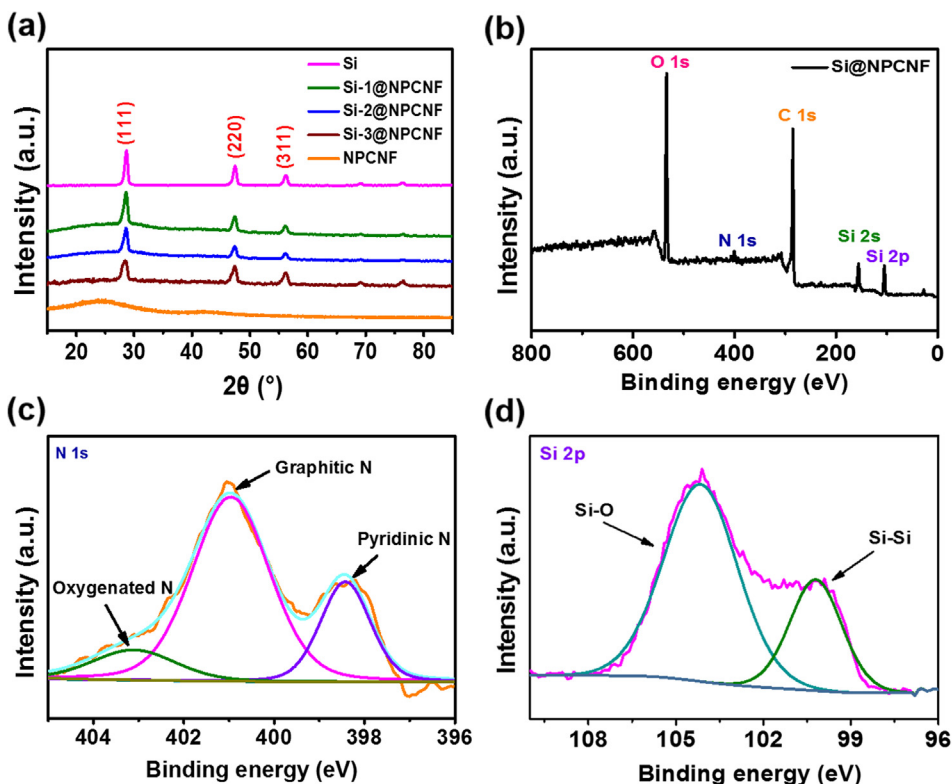
Fig. 5. (a) XRD patterns of Si nanoparticles, NPCNF, and Si@NPCNF composites. XPS spectra of the Si-2@NPCNF composite: (b) survey spectrum, (c) N 1s, (d) Si 2p.
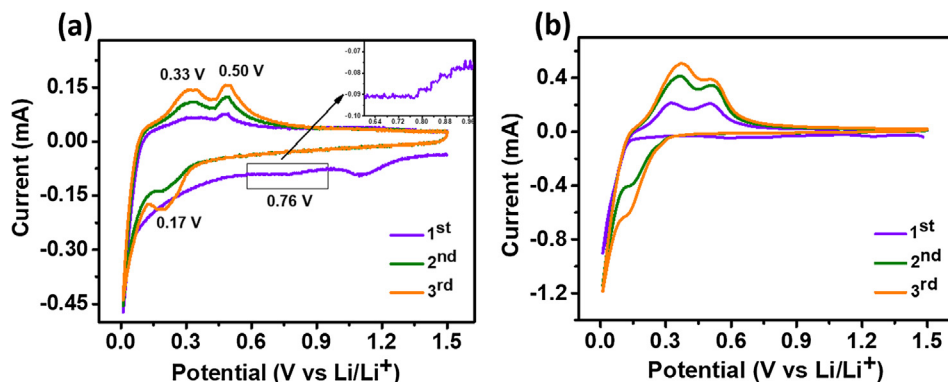

Fig. 6. CV curves of (a) Si-2@NPCNF and (b) Si nanoparticle anodes at the first three cycles.

bath and decomposition of PMMA during the thermal treatment process. The corresponding higher-magnification TEM images clearly demonstrate the spacing of 0.31 nm for the spherical Si nanoparticles with a diameter around 30 nm (Fig. 4c and 4d), being in consistent with the (1 1 1) plane of Si [36,37]. Therefore, it is a clear evidence that the Si@NPCNF composite with designed porous structures have been realized by the novel electrospinning strategy combined with an in-situ reaction collection bath.

Determined by the N_2 adsorption/desorption isotherms (Fig. S2a), the BET surface areas of Si-2@NPCNF and NPCNF are calculated to be 118.9 and 78.4 $m^2 g^{-1}$, respectively. Additionally, the total pore volume of Si-2@NPCNF is 0.286 $cm^3 g^{-1}$ with the pore size distribution ranging from 3 nm to 24 nm as displayed in Fig. S2b, suggesting that the Si-2@NPCNF composite mainly owns a mesoporous structure. The large surface area of Si-2@NPCNF is expected to efficiently shorten the distance of lithium-ion diffusion and promote the penetration of electrolyte by providing sufficient electrode/electrolyte interfaces. Meanwhile, the Si-2@NPCNF composite with high porosity is even anticipated to effectively accommodate the severe volumetric changes of Si during the

lithiation/delithiation processes, thus leading to improved cycling performance [38–40]. As further measured in Fig. S3, the contents of Si in Si-1@NPCNF, Si-2@NPCNF and Si-3@NPCNF composites are calculated to be 34.3%, 48.8% and 60.5%, respectively.

Fig. 5a shows the XRD patterns of Si nanoparticles, NPCNF, and Si@NPCNF composites. Characteristic diffraction peaks at 2θ = 28.5, 47.4, 56.2, 69.3 and 76.2° are observed for all the Si@NPCNF composites, which correspond to the (1 1 1), (2 2 0), (3 1 1), (4 0 0) and (3 3 1) planes of the crystalline silicon phase, respectively. It also indicates that Si nanoparticles are very stable during the electrospinning, in-situ polymerization of PPy and high-temperature carbonization processes [41]. The chemical compositions of the Si@NPCNF composite are analyzed by XPS as depicted in Fig. 5b. The five peaks observed at 102.3, 152.2, 284.2, 400.1 and 533.5 eV are assigned to the Si 2p, Si 2s, C 1s, N 1s, and O 1s, respectively [12]. According to Fig. 5c, the high-resolution N 1s spectrum can be divided and fitted into three sub-peaks at 398.4, 401.0, and 403.1 eV, which are specified as the pyridinic-N, graphitic-N, and oxygenated-N in the porous carbon fibers [42]. This further demonstrates that PPy can be served as both the conductive
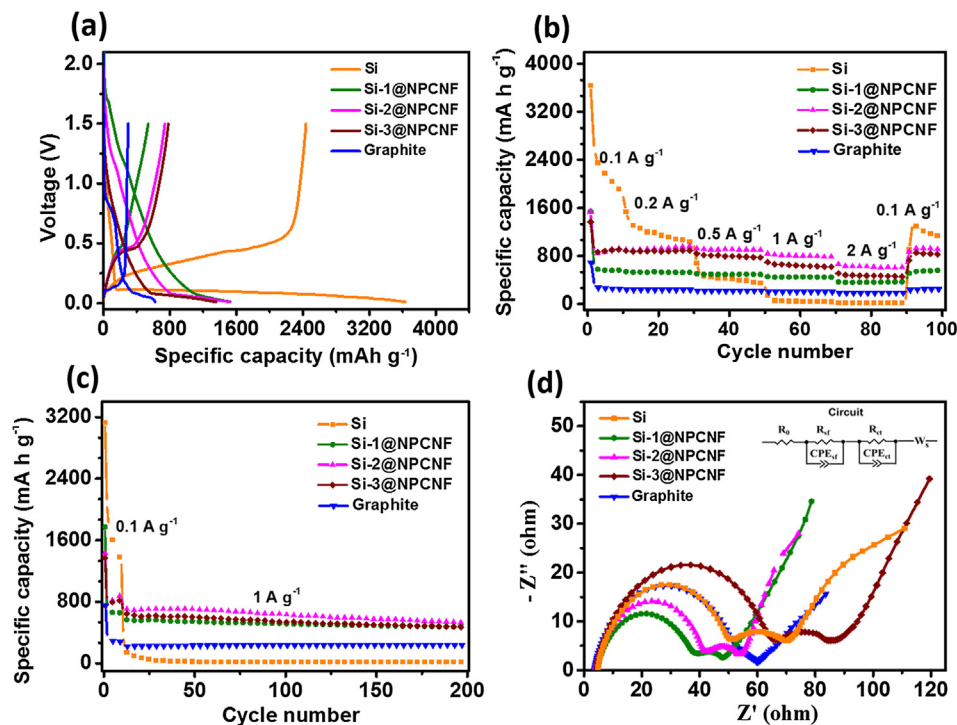
Fig. 7. (a) Galvanostatic discharge/charge profiles, (b) rate performance, (c) cycling performance, and (d) EIS plots of Si, Si@NPCNF and NPCNF anodes.

carbon matrix and nitrogen resource to form the N-doped carbonaceous framework [43]. The Si 2p spectra (Fig. 5d) reveals the sub-peaks of the Si−Si band indexed to metallic Si and the Si−O band which may be caused by the slight oxidation of Si nanoparticles in air.

The porous structure of Si@NPCNF composites are expected to effectively relieve the severe volume expansion of silicon nanoparticles [44]. Hence, Si@NPCNF nanocomposites with various Si contents are used as anode materials to assemble coin-cell LIBs. CV curves of Si nanoparticles and Si@NPCNF composites for the first three cycles are achieved in the voltage range between 0.01 and 1.5 V at a scanning rate of 0.1 mV s^{-1} (Fig. 6 and S4). A broad cathodic peak appears around 0.76 V in the first cycle of Si@NPCNF nanocomposites and then disappears in the latter cycles (Fig. 6a and S4), which results from the electrolyte decomposition accompanying the formation of the SEI films. Then, another cathodic peak is observed at 0.17 V from the second cycle, indicating the corresponding lithiation reaction of Si to form Li$_x$Si alloys. The sharp peak on the verge of the cut-off potential is attributed to the lithiation of the carbon layer and Si nanoparticles [45]. Meanwhile, the two distinct peaks at about 0.33 V and 0.50 V during the anodic sweep can be ascribed to the delithiation of Li$_x$Si to form amorphous-phase Si [33]. In the subsequent cycles, the representative discharge/charge profiles of amorphous Si are exhibited, being consistent with the previous reports [46,47].

Fig. 7a shows the first-cycle galvanostatic discharge/charge profiles of Si nanoparticles, Si-1@NPCNF, Si-2@NPCNF, Si-3@NPCNF and graphite anodes at a current density of 0.1 A g^{-1}. It has been demonstrated that the initial lithiation of crystalline Si results in a low voltage plateau around 0.15 V corresponding to a two-phase region in which Li$_x$Si is formed while the delithiation of Li$_x$Si results in a plateau at 0.35 V corresponding to the formation of delithiated amorphous Si [35]. The initial discharge capacities of pure Si nanoparticles, Si-1@ NPCNF, Si-2@NPCNF, Si-3@NPCNF and graphite anodes are 3637, 1528, 1521, 1354, and 620 mA h g^{-1}, with the initial coulombic efficiencies of 63.4%, 38.5%, 54.4%, 67.0%, and 48.1% respectively. Such a large capacity loss can be mainly stemmed from the formation of the SEI layer on the electrode surface as well as the dealloyed Li which disintegrates from the SEI layer during the discharge process [35,40].

Fig. 7b shows the corresponding rate performances of Si nanoparticles, Si-1@NPCNF, Si-2@NPCNF, Si-3@NPCNF and graphite. For the pure Si nanoparticle anode, although it shows a rather high discharge capacity of 3637 mA h g^{-1} at 0.1 A g^{-1}, there is only a low retention (0.1%) of the initial capacity at the high current density of 2 A g^{-1} due to the large volume changes upon cycling. Compared with the graphite anode, the Si-2@NPCNF electrode delivers higher reversible capacities of 1521, 921, 910, 822, and 647 mA h g^{-1} at the current densities of 0.1, 0.2, 0.5, 1.0, and 2.0 A g^{-1}, respectively. Additionally, when the discharge/charge density drops back to 0.1 A g^{-1}, the capacity of Si-2@ NPCNF can return to 923 mA h g^{-1} which is much higher than that of graphite (237 mA h g^{-1}).

The cycling stability is another crucial indicator for lithium-ion batteries besides the high discharge capacity and good rate performance. Hence, the cycling performances of Si nanoparticles, Si-1@ NPCNF, Si-2@NPCNF, Si-3@NPCNF and graphite were carried out at a current density of 1 A g^{-1}. As exhibited in Fig. 7c, stable capacities of 1.1, 462.9, 515.5, 455.0, and 239.1 mA h g^{-1} with retentions of 0.3%, 74.0%, 80.0%, 70.2%, and 104.4% are obtained after 200 cycles at 1 A g^{-1} for Si nanoparticles, Si-1@NPCNF, Si-2@NPCNF, Si-3@NPCNF and graphite electrodes, respectively. The Si@NPCNF nanocomposites present much better cycling stability and rate performances, further indicating that the designed porous nitrogen-doped carbonaceous architectures derived from the one-step removal of PVP and in-situ polymerization of PPy could serve as an efficient buffering matrix to stabilize the active Si phases and enhance the electrical conductivity of the whole electrode. Ultimately, significantly increased cycling and rate performances are achieved [48,49].

Electrochemical impedance spectroscopy (EIS) measurements were further adopted to analyze the underlying discharge/charge kinetics of Si nanoparticles, Si-1@NPCNF, Si-2@NPCNF, Si-3@NPCNF and graphite. As presented in Fig. 7d, the Nyquist plots are qualitatively analyzed by Z-view software with the simulation results presented in Table S1. As is shown, R$_O$ is the equivalent series resistance which generally describes the resistance of the electrolyte combined with the internal resistance of the electrode, while R$_{sf}$ and R$_{ct}$ correspond to the SEI film resistance (first high-frequency semicircle) and the charge transfer

resistance (second semicircle), respectively [50]. The R$_{ct}$ values of Si-1@NPCNF (11.18 Ω), Si-2@NPCNF (12.02 Ω), and Si-3@NPCNF (13.78 Ω) were much smaller than that (45.41 Ω) of Si, meaning that the presence of carbon fiber can significantly reduce the charge transfer resistance which is favorable for reducing polarization of the electrode and accelerating alloying/dealloying reaction kinetics as well. Similarly, the larger slope of the straight line in the Si@NPCNF composites represents a faster diffusion controlled process in the solid electrode compared to the Si anode, further indicating that the incorporation of the 3D porous carbon fiber framework significantly improves the transport of Li$^+$ during discharge/charge cycles.

4. Conclusions

In summary, we have successfully obtained a Si @ nitrogen-doped porous carbon fiber composite by a facile electrospinning strategy combined with a unique in-situ reaction bath of pyrrole monomer as the collector. The specific design can simultaneously achieve the acquisition of porous Si/PMMA fibers through the dissolution of PVP phase, and the in-situ polymerization of PPy on the surface of porous Si/PMMA fiber as well. Thus, the mesoporous structure is totally duplicated by the PPy-derived NPCNF framework with high porosity and good conductivity after carbonization, which can effectively buffer the volume changes of Si nanoparticles as well as provide facilitated Li$^+$ diffusion and electron transfer pathway for the alloying/dealloying processes. As a result, the Si@NPCNF composite as a lithium-ion battery anode material exhibits a high initial capacity of 1521 mA h g^{-1} at 0.1 A g^{-1}, and an outstanding cycle stability of 515.5 mA h g^{-1} after 200 cycles under the current density of 1 A g^{-1}.

Acknowledgements

Appendix A. Supplementary material

Supplementary data to this article can be found online at https://doi.org/10.1016/j.apsusc.2018.12.172.

References

[1] B. Scrosati, J. Hassoun, Y.K. Sun, Lithium-ion batteries. A look into the future, Energy Environ. Sci. 4 (2011) 3287–3295.
[2] R. Marom, S.F. Amalraj, N. Leifer, D. Jacob, D. Aurbach, A review of advanced and practical lithium battery materials, J. Mater. Chem. 21 (2011) 9938–9954.
[3] Z.L. Xu, J.K. Kim, K. Kang, Carbon nanomaterials for advanced lithium sulfur batteries, Nano Today 19 (2018) 84–107.
[4] J. Wang, H. Tang, L. Zhang, H. Ren, R. Yu, Q. Jin, J. Qi, D. Mao, M. Yang, Y. Wang, P. Liu, Y. Zhang, Y. Wen, L. Gu, G. Ma, Z. Su, Z. Tang, H. Zhao, D. Wang, Multi-shelled metal oxides prepared via an anion-adsorption mechanism for lithium-ion batteries, Nat. Energy 1 (2016) 16050.
[5] H. Wu, G. Yu, L. Pan, N. Liu, M.T. McDowell, Z. Bao, Y. Cui, Stable Li-ion battery anodes by in-situ polymerization of conducting hydrogel to conformally coat silicon nanoparticles, Nat. Commun. 4 (2013) 1943.
[6] V. Singh, D. Joung, L. Zhai, S. Das, S.I. Khondaker, S. Seal, Graphene based materials: past, present and future, Prog. Mater. Sci. 56 (2011) 1178–1271.
[7] E. Yoo, J. Kim, E. Hosono, H.S. Zhou, T. Kudo, I. Honma, Large reversible Li storage of graphene nanosheet families for use in rechargeable lithium-ion batteries, Nano Lett. 8 (2008) 2277–2282.
[8] Z.S. Wu, W. Ren, L. Wen, L. Gao, J. Zhao, Z. Chen, G. Zhou, F. Li, H.M. Cheng, Graphene anchored with Co3O4 nanoparticles as anode of lithium-ion batteries with enhanced reversible capacity and cyclic performance, ACS Nano 4 (2010) 3187–3194.
[9] V. Etacheri, R. Marom, R. Elazari, G. Salitra, D. Aurbach, Challenges in the

[10] development of advanced Li-ion batteries: a review, Energy Environ. Sci. 4 (2011) 3243.
[11] J.B. Goodenough, Y. Kim, Challenges for rechargeable Li batteries, Chem. Mater. 22 (2010) 587–603.
[12] C.K. Chan, H. Peng, G. Liu, K. McIlwrath, X.F. Zhang, R.A. Huggins, Y. Cui, High-performance lithium battery anodes using silicon nanowires, Nat. Nanotechnol. 3 (2008) 31–35.
[13] H. Kim, B. Han, J. Choo, J. Cho, Three-dimensional porous silicon particles for use in high-performance lithium secondary batteries, Angew. Chem. Int. Ed. 47 (2008) 10151–10154.
[14] H. Li, X.J. Huang, L.Q. Chen, Z.G. Wu, Y. Liang, A high capacity nano-Si composite anode material for lithium rechargeable batteries, Electrochem. Solid State Lett. 2 (1999) 547–549.
[15] J.P. Maranchi, A.F. Hepp, P.N. Kumta, High capacity, reversible silicon thin-film anodes for lithium-ion batteries, Electrochem. Solid State Lett. 6 (2003) A198–A201.
[16] X. Su, Q. Wu, J. Li, X. Xiao, A. Lott, W. Lu, B.W. Sheldon, J. Wu, Silicon-based nanomaterials for lithium-ion batteries: a review, Adv. Energy Mater. 4 (2014) 1300882.
[17] L. Liu, J. Lyu, T. Li, T. Zhao, Well-constructed silicon-based materials as high-performance lithium-ion battery anodes, Nanoscale 8 (2016) 701–722.
[18] A. Mukhopadhyay, B.W. Sheldon, Deformation and stress in electrode materials for Li-ion batteries, Prog. Mater. Sci. 63 (2014) 58–116.
[19] J.R. Szczech, S. Jin, Nanostructured silicon for high capacity lithium battery anodes, Energy Environ. Sci. 4 (2011) 56–72.
[20] K. Feng, M. Li, W. Liu, A.G. Kashkooli, X. Xiao, M. Cai, Z. Chen, Silicon-based anodes for lithium-ion batteries: from fundamentals to practical applications, Small 14 (2018) 1702737.
[21] W. Li, Q. Wang, K. Cao, J. Tang, H. Wang, L. Zhou, H. Yao, Mechanics-based optimization of yolk-shell carbon-coated silicon nanoparticle as electrode materials for high-capacity lithium ion battery, Compos. Commun. 1 (2016) 1–5.
[22] N. Liu, Z. Lu, J. Zhao, M.T. Mcdowell, H.W. Lee, W. Zhao, Y. Cui, A pomegranate-inspired nanoscale design for large-volume-change lithium battery anodes, Nat. Nanotechnol. 9 (2014) 187–192.
[23] Z.L. Xu, X. Liu, Y. Luo, L. Zhou, J.K. Kim, Nanosilicon anodes for high performance rechargeable batteries, Prog. Mater. Sci. 90 (2017) 1–44.
[24] J. Graetz, C.C. Ahn, R. Yazami, B. Fultz, Highly reversible lithium storage in nanostructured silicon, Electrochem. Solid State Lett. 6 (2003) A194–A197.
[25] Z.L. Xu, K. Cao, S. Abouali, M. Akbari Garakani, J. Huang, J.Q. Huang, E. Kamali Heidari, H. Wang, J.K. Kim, Study of lithiation mechanisms of high performance carbon-coated Si anodes by in-situ microscopy, Energy Storage Mater. 3 (2016) 45–54.
[26] M.N. Obrovac, V.L. Chevrier, Alloy negative electrodes for Li-ion batteries, Chem. Rev. 114 (2014) 11444–11502.
[27] L.F. Cui, L. Hu, J.W. Choi, Y. Cui, Light-weight free-standing carbon nanotube-silicon films for anodes of lithium-ion batteries, ACS Nano 4 (2010) 3671–3678.
[28] L.F. Cui, Y. Yang, C.M. Hsu, Y. Cui, Carbon-silicon core-shell nanowires as high capacity electrode for lithium-ion batteries, Nano Lett. 9 (2009) 3370–3374.
[29] M.L. Terranova, S. Orlanducci, E. Tamburri, V. Guglielmotti, M. Rossi, Si/C hybrid nanostructures for Li-ion anodes: an overview, J. Power Sources 246 (2014) 167–177.
[30] W. Wang, P.N. Kumta, Nanostructured hybrid silicon/carbon nanotube heterostructures: reversible high-capacity lithium-ion anodes, ACS Nano 4 (2010) 2233–2241.
[31] S. Jiang, Y. Chen, G. Duan, C. Mei, A. Greiner, S. Agarwal, Electrospun nanofiber reinforced composites: a review, Polym. Chem. 9 (2018) 2685–2720.
[32] H. Li, H. Zhou, Enhancing the performances of Li-ion batteries by carbon-coating: present and future, Chem. Commun. 48 (2012) 1201–1217.
[33] S.Y. Chew, Z.P. Guo, J.Z. Wang, J. Chen, P. Munroe, S.H. Ng, L. Zhao, H.K. Liu, Novel nano-silicon/polypyrrole composites for lithium storage, Electrochem. Commun. 9 (2007) 941–946.
[34] Z. Du, S. Zhang, Y. Liu, J. Zhao, R. Lin, T. Jiang, Facile fabrication of reticular polypyrrole-silicon core-shell nanofibers for high performance lithium storage, J. Mater. Chem. 22 (2012) 11636–11641.
[35] Z.P. Guo, J.Z. Wang, H.K. Liu, S.X. Dou, Study of silicon/polypyrrole composite as anode material for Li-ion batteries, J. Power Sources 146 (2005) 448–451.
[36] X.Y. Zhou, J.J. Tang, J. Yang, Y.L. Zou, S.C. Wang, J. Xie, L.L. Ma, Effect of polypyrrole on improving electrochemical performance of silicon based anode materials, Electrochim. Acta 70 (2012) 296–303.
[37] I. Kang, J. Jang, M.S. Kim, J.W. Park, J.H. Kim, Y.W. Cho, Nanostructured silicon/silicide/carbon composite anodes with controllable voids for Li-ion batteries, Mater. Design 120 (2017) 230–237.
[38] T. Jaumann, M. Gerwig, J. Balach, S. Oswald, E. Brendler, R. Hauser, B. Kieback, J. Eckert, L. Giebeler, E. Kroke, Dichlorosilane-derived nano-silicon inside hollow carbon spheres as a high-performance anode for Li-ion batteries, J. Mater. Chem. A 5 (2017) 9262–9271.
[39] X. Huang, X. Sui, H. Yang, R. Ren, Y. Wu, X. Guo, J. Chen, HF-free synthesis of Si/C yolk/shell anodes for lithium-ion batteries, J. Mater. Chem. A 6 (2018) 2593–2599.
[40] G. Liang, X. Qin, J. Zou, L. Luo, Y. Wang, M. Wu, H. Zhu, G. Chen, F. Kang, B. Li, Electrosprayed silicon-embedded porous carbon microspheres as lithium-ion battery anodes with exceptional rate capacities, Carbon 127 (2018) 424–431.
[41] S. Chen, Z. Chen, X. Xu, C. Cao, M. Xia, Y. Luo, Scalable 2D mesoporous silicon nanosheets for high-performance lithium-ion battery anode, Small 14 (2018) 1703361.
[42] S. Guo, X. Hu, Y. Hou, Z. Wen, Tunable synthesis of yolk-shell porous silicon@carbon for optimizing Si/C-based anode of lithium-ion batteries, ACS Appl. Mater.

Interfaces 9 (2017) 42084–42092.

[42] S. Cai, Z. Meng, H. Tang, Y. Wang, P. Tsiakaras, 3D Co-N-doped hollow carbon spheres as excellent bifunctional electrocatalysts for oxygen reduction reaction and oxygen evolution reaction, Appl. Catal. B 217 (2017) 477–484.

[43] B. Lu, B. Ma, X. Deng, W. Li, Z. Wu, H. Shu, X. Wang, Cornlike ordered mesoporous silicon particles modified by nitrogen-doped carbon layer for the application of Li-Ion battery, ACS Appl. Mater. Interfaces 9 (2017) 32829–32839.

[44] J. Li, J. Huang, A nanofibrous polypyrrole/silicon composite derived from cellulose substance as the anode material for lithium-ion batteries, Chem. Commun. 51 (2015) 14590–14593.

[45] J. Li, J. Wang, J. Yang, X. Ma, S. Lu, Scalable synthesis of a novel structured graphite/silicon/pyrolyzed-carbon composite as anode material for high-performance lithium-ion batteries, J. Alloys Compd. 688 (2016) 1072–1079.

[46] Y.C. Zhang, Y. You, S. Xin, Y.X. Yin, J. Zhang, P. Wang, X.S. Zheng, F.F. Cao, Y.G. Guo, Rice husk-derived hierarchical silicon/nitrogen-doped carbon/carbon nanotube spheres as low-cost and high-capacity anodes for lithium-ion batteries, Nano Energy 25 (2016) 120–127.

[47] Y. Xu, Y. Zhu, F. Han, C. Luo, C. Wang, 3D Si/C fiber paper electrodes fabricated using a combined electrospray/electrospinning technique for Li-Ion batteries, Adv. Energy Mater. 5 (2015) 1400753.

[48] J. Ryu, D. Hong, S. Choi, S. Park, Synthesis of ultrathin Si nanosheets from natural clays for Lithium-Ion battery anodes, ACS Nano 10 (2016) 2843–2851.

[49] Z.Q. Wen, M. Li, S.J. Zhu, T. Wang, Novel mesoporous carbon-carbonaceous materials nanostructures decorated with MnO_2 nanosheets for supercapacitors, Int. J. Electrochem. Sci. 11 (2016) 1810–1820.

[50] Z.L. Xu, J.Q. Huang, W.G. Chong, X. Qin, X. Wang, L. Zhou, J.K. Kim, In situ TEM study of volume expansion in porous carbon nanofiber/sulfur cathodes with exceptional high-rate performance, Adv. Energy Mater. 7 (2017) 1602078.